AFRL-AFOSR-VA-TR-2021-0061

RTB1-Computational-Experimental Reactive Wetting of Hf-Ti-Me Alloy Melts with B4C

Arturo Bronson
UNIVERSITY OF TEXAS AT EL PASO
500 W UNIVERSITY AVE
EL PASO, TX, 79968
USA

06/27/2021
Final Technical Report

Air Force Research Laboratory
Air Force Office of Scientific Research
Arlington, Virginia 22203
Air Force Materiel Command

REPORT DOCUMENTATION PAGE

Form Approved
OMB No. 0704-0188

1. REPORT DATE *(DD-MM-YYYY)*	**2. REPORT TYPE**	**3. DATES COVERED** *(From - To)*
27-06-2021	Final	15 Aug 2017 - 31 Dec 2020

4. TITLE AND SUBTITLE
RTB1-Computational-Experimental Reactive Wetting of Hf-Ti-Me Alloy Melts with B4C

5a. CONTRACT NUMBER

5b. GRANT NUMBER
FA9550-17-1-0393

5c. PROGRAM ELEMENT NUMBER
61102F

6. AUTHOR(S)
Arturo Bronson

5d. PROJECT NUMBER

5e. TASK NUMBER

5f. WORK UNIT NUMBER

7. PERFORMING ORGANIZATION NAME(S) AND ADDRESS(ES)
UNIVERSITY OF TEXAS AT EL PASO
500 W UNIVERSITY AVE
EL PASO, TX 79968
USA

8. PERFORMING ORGANIZATION REPORT NUMBER

9. SPONSORING/MONITORING AGENCY NAME(S) AND ADDRESS(ES)
AF Office of Scientific Research
875 N. Randolph St. Room 3112
Arlington, VA 22203

10. SPONSOR/MONITOR'S ACRONYM(S)
AFRL/AFOSR RTB1

11. SPONSOR/MONITOR'S REPORT NUMBER(S)
AFRL-AFOSR-VA-TR-2021-0061

12. DISTRIBUTION/AVAILABILITY STATEMENT
A Distribution Unlimited: PB Public Release

13. SUPPLEMENTARY NOTES

14. ABSTRACT
This research project investigates the processing of Hf-Ti-Nb alloy melts with B4C to form boride-carbide precipitates in a Hf-Ti-Nb alloy matrix. The objective of the proposed research is to study the (Hf-Ti-Nb)Liq/B4C processing driven by computational fluid dynamics (CFD) and computational thermodynamics through the following three integrated research thrusts: Investigate the use of surface tensions of liquid Hf-Ti-Nb alloys to predict their infusion into a B4C packed bed by computational fluid dynamics at 2800 K (2527°C); Investigate the effect of the temperature gradient on the fluid dynamics: Investigate the reaction path of (Hf-Ti-Nb)Liq/B4C through the microstructures.

15. SUBJECT TERMS

16. SECURITY CLASSIFICATION OF:			**17. LIMITATION OF ABSTRACT**	**18. NUMBER OF PAGES**	**19a. NAME OF RESPONSIBLE PERSON**
a. REPORT	**b. ABSTRACT**	**c. THIS PAGE**			ALI SAYIR
U	U	U	UU	21	**19b. TELEPHONE NUMBER** *(Include area code)* 426-7236

Standard Form 298 (Rev.8/98)
Prescribed by ANSI Std. Z39.18

PROGRESS REPORT

for the

Research Project
(AFOSR Award Number – FA9550-17-1-0393)

Entitled

Computational – Experimental Reactive Wetting of Hf-Ti-Me Alloy Melts with B_4C

By

Arturo Bronson and Vinod Kumar
Department of Mechanical Engineering
University of Texas at El Paso

March 31, 2021

Computational – Experimental Reactive Wetting of Hf-Ti-Me Alloy Melts with B_4C

Arturo Bronson and Vinod Kumar, The University of Texas at El Paso

Project Summary

This research project investigates the processing of Hf-Ti-Nb alloy melts with B_4C to form boride-carbide precipitates in a Hf-Ti-Nb alloy matrix. Although the ultimate goal of the research endeavor is to enhance significantly the oxidation resistance of ultrahigh temperature ceramic composites (UHTCC), the processing of these reactive metals must be improved dramatically to control the eventual development of the oxide scale. **The objective of the proposed research is to study the $(Hf\text{-}Ti\text{-}Nb)_{Liq}/B_4C$ processing driven by computational fluid dynamics (CFD) and computational thermodynamics through the following three integrated research thrusts:**

- Investigate the use of surface tensions of liquid Hf-Ti-Nb alloys to predict their infusion into a B_4C packed bed by computational fluid dynamics at 2800 K (2527°C);
- Investigate the effect of the temperature gradient on the fluid dynamics, as well as the stable and metastable phases within the boride-carbide/Hf alloy composite.
- Investigate the reaction path of $(Hf\text{-}Ti\text{-}Nb)_{Liq}/B_4C$ through the microstructures formed at temperatures greater than 2800 K (2527°C) toward controlling the precipitation.

The surface tension of the alloy melt will be linked to the depth of melt penetration and the segregation of the alloying elements (i.e., Hf, Ti and Nb) within the pores. The segregation can then be exploited to place elements for developing a protective oxidizing scale as the composite oxidizes. **With an understanding of the fluid dynamics of the Hf alloy melt through varying-spatial pore channels, the elemental components should segregate the carbide and boride phases creating a directional microstructure causing a tactical development of the scale interphase upon oxidation.**

1. Introduction

Ceramic composites and intermetallics have become the core materials to meet the strength and extreme temperature needed for gas-turbine engines and hypersonic aerosurfaces[1] The successful integration of an ultrahigh-temperature, ceramic composite (UHTCC) for these applications requires careful and optimal consideration of processing, mechanics and oxidation. The research focuses on predicting the fluid flow of liquid melts from mainly the Hf family (i.e., Hf and Ti) into a packed bed of B_4C. During infiltration, reactions between the Hf-Nb-Ti alloy melt and B_4C will form an HfB_2-HfC/Hf-Ti-Nb composite, which may eventually develop oxide layers of HfO_2-TiO_2- Nb_2O_5, HfO_2-TiO_2 and TiO_2.

On a previous study, the computational-experimental approach was used to investigate the effects of thermal mismatch and growth stresses on the ZrB_2/ZrC/Zr-Si system[2]. However, the operational boundaries must be pushed by using rutile instead of silica to control vaporization[3] and Hf components rather than Zr compounds to attain better ultrahigh temperature performance. In addition, to acquire the ultimate Hf protective-scale system, the processing of the Hf melts with B_4C must be better controlled.

2. Status of Effort

2.1. Computational Effort on the Liquid Metal Infusion into a Packed Bed **-** In this section the computational effort is only summarized. A full paper is in its final form for submittal to Metallurgical and Materials Transactions B has been appended.

In considering the dynamic wetting of liquid metal infusion into a packed bed, the effect of the contact angle on the penetrating rate and distance was analyzed by examining the momentum balance of the liquid within a capillary, as well as the initial movement assuming a reactionary front. A numerical solution for liquid Ti infusing into a 10 μm radius, cylindrical capillary was determined as a function of contact angle for a non-reactive case with initial and final contact angles of 80°and 0°, respectively. If the reactive front of liquid Ti on a substrate is assumed to depend on the rate-determining step of the adsorption of Ti onto a surface defect (e.g., vacancy), the contact angle becomes controlled by the rate constant of the reaction for adsorption. The maximum velocity of the imbibing rate of liquid Ti into a capillary occurs near 1 μs and depends on the contact angle though the meniscus velocity for liquid Ti infusion decreases slightly with increasing contact-line friction at the liquid/substrate interface. For the interactions among the contact angle, contact-line friction and the adsorption of Ti onto the surface adjacent to the advancing liquid front, the contact angle appears to contribute the most to the imbibing rate.

The terms for forces of inertia and end-drag contribute as dramatically as the surface tension at infusing times less than 1 μs. As a consequence, the end effects and the wetting- or contact-line friction was expected to change the maximum velocity. Without a contact-line friction, the maximum velocity for penetration occurring near 1 μs decreases with increasing contact angle between liquid Ti and the substrate. The meniscus velocity for liquid Ti infusion decreases with increasing contact-line friction at the liquid/substrate interface. The interfacial interactions suggest that the contact line friction becomes a contributory factor in the μm and nm scale affecting nanomaterial processing.

The adsorption of atoms onto the surface from the liquid phase becomes an equally contributing factor. The adsorbed species (i.e., $n_{Ti,Ads}$) is directly related to the thermodynamic activity of a liquid component (e.g., a_{Ti}), which affects obviously the surface tension. Although the Gibbs adsorption isotherm is not the focus in the present study, the adsorbed species contributes to the surface tension. However, the maximum height increases with decreasing time-constant, which is the reciprocal of the rate constant as developed in the appended manuscript. The maximum velocity decreases slightly with increasing the end-effect parameter but seems to affect the imbibing rate less than the contact line friction and the rate of reaction. A full explanation of our analysis of the effect of the fluid mechanics and reaction for Ti adsorption on the contact angle is described in the appended manuscript.

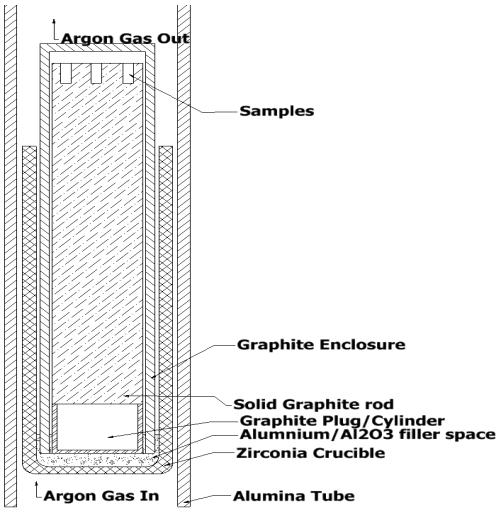

Figure 1 -- Sketch of graphite enclosure used to infuse experimentally Hf-Y-Ti melts into B_4C

2.2. Experimental Study on the Infusion of Hf-Ti-Nb alloys into B_4C: The previous processing technique of infusing liquid Zr-Si alloys into B_4C was changed to study Hf-Nb-Ti melts into a B_4C packed bed. A graphite enclosure will be used for the processing of the composite, as shown in Figure 1. The samples were previously placed at the top part of the graphite crucible packed with a B_4C bed maintained in the hot zone of the furnace

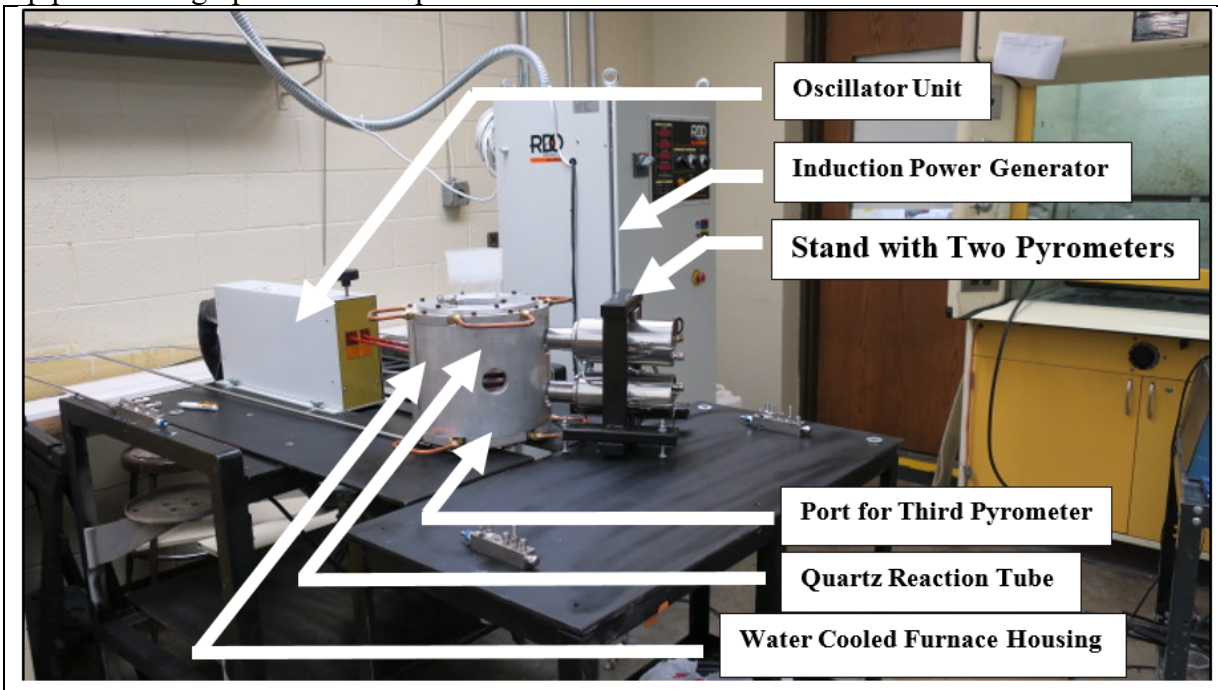

Figure 2 -- Induction Furnace Facility with major components identified.

(i.e., 1750°C). The configuration has an hot zone for the experimental temperature and a cold zone. If needed, our present study will use a cold zone to fix the oxygen potential with the Al-C-

O system. The CO generated from the residual oxygen within the enclosure will serve as a carrier gas pulling oxygen from the hot zone to the cold zone. Towards the bottom is the zone where the Al melt seals the crucible thus controlling the oxidation potential within the graphite enclosure serving as a closed thermodynamic system. For example, the oxidation potential of 10^{-47} atm will be fixed at the triple point of $Al/Al_2O_3/Al_4CO_4$. Although the previous experimental configuration was used for the study of Al-Sm-Me alloys by Dr. Shantha-Kumar,[37] the present study may have the liquid Al at the top of enclosure because the temperature in the furnace shown in Figures 2 and 3 is hotter at the bottom.

The major components of the induction furnace facility are completed, as shown in Figure 3. The furnace housing has three openings for pyrometers to determine temperature gradients developed axially and radially from exothermic reactions resulting from the liquid Hf alloys

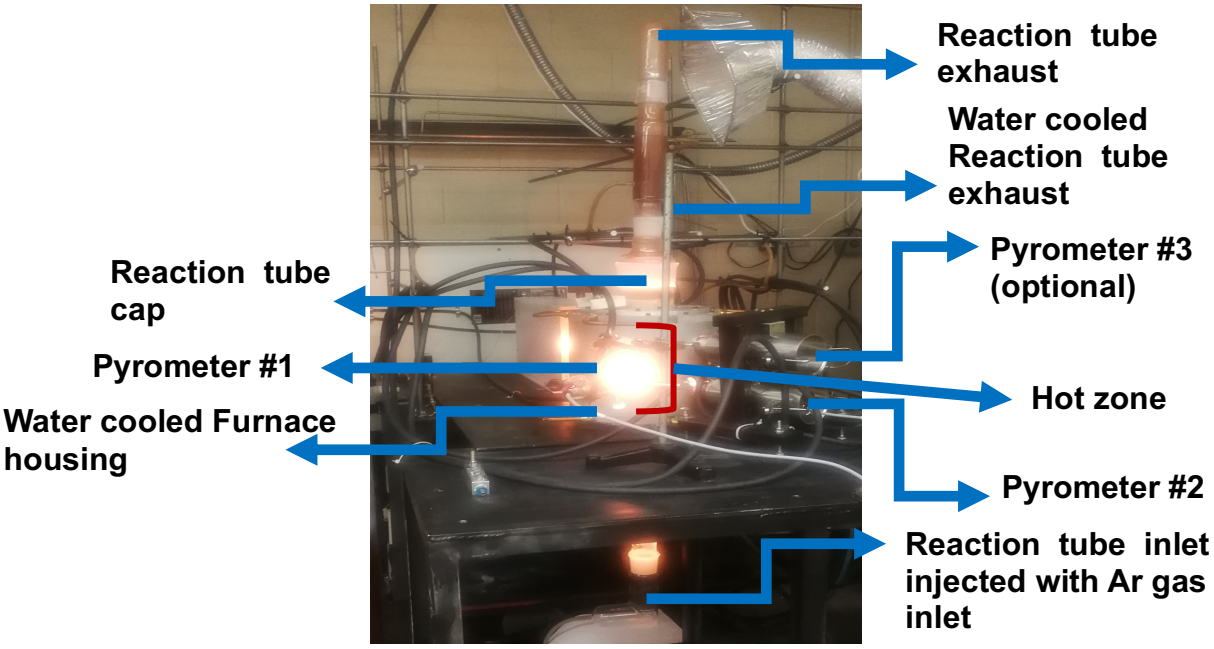

Figure 3 -- Ultra-high temperature operation

contacting the B_4C packed bed. The major effort is determining the temperature of the B_4C bed, liquid Hf-Ti-Nb alloy and the liquid alloy with B_4C, so the experimental configurations were designed as shown in Figure 2 and 3.

Graphite crucibles were used to hold liquid metal and allowed to drain into the surrounding annulus which contained B_4C particles of 1 to 10 μm size. The temperature extremes generated from temperatures exceeding 2000°C at the center of the packed bed may synthesize metastable ternary and quaternary compounds. The heat and mass transfer will also generate temperature and concentration distributions expected to affect microstructures within the HfB_2-HfC/Hf-Ti-Nb composite. As determined by the experimental results of Nb/B_4C, the Nb melted indicating a temperature of greater than 2477°C was achieved. Hence, the researcher devoted time to measure accurately the temperature outside and inside the graphite crucibles containing the metal or alloys placed on top of the B_4C packed bed, as explained in section 2.4 of the report. An improved technique is obviously needed on carefully placing and aligning the pyrometers to sighting cavities.

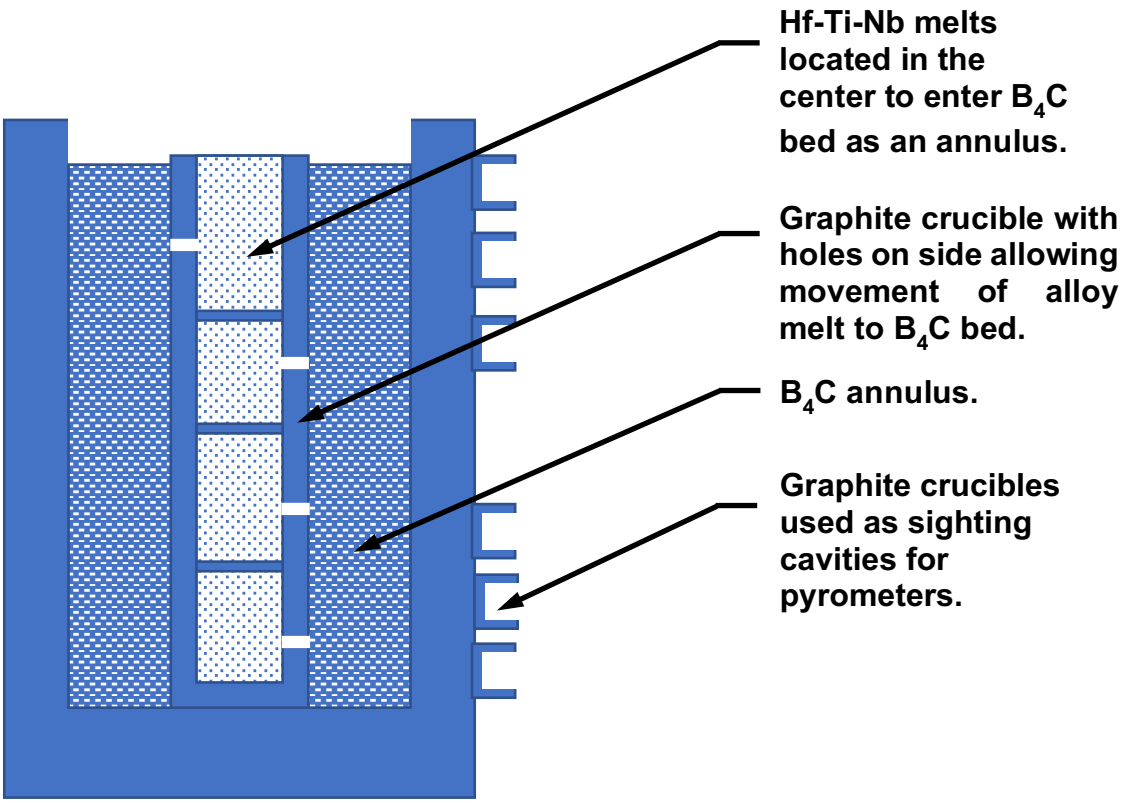

Figure 4 -- Experimental configuration for Hf-Nb-Ti liquid reacting with B_4C.

Besides the surface tension controlling the penetration rate of liquid infusion, the contact angle has an integral part. Although the contact angle governing the liquid/solid interfacial surface tension may range for 0 to 1 as a result of the cos θ incorporated in the force term for the surface tension, the penetrating rate or velocity would decrease. The contact angle will obviously affect the depth of penetration (h) with the contact angle ranging from 0 to 80°.

2.3. Microstructural Observations of Hf Liquid Alloys Reacting with B_4C – Experimental runs were performed with metal contained in graphite crucibles with a side hole allowing liquid metal to flow into the annulus containing B_4C. This experimental configuration gave an obvious indication that the metal did not oxidize, but the XRD should provide a definite check that the oxygen potential without a cold zone was sufficiently low to

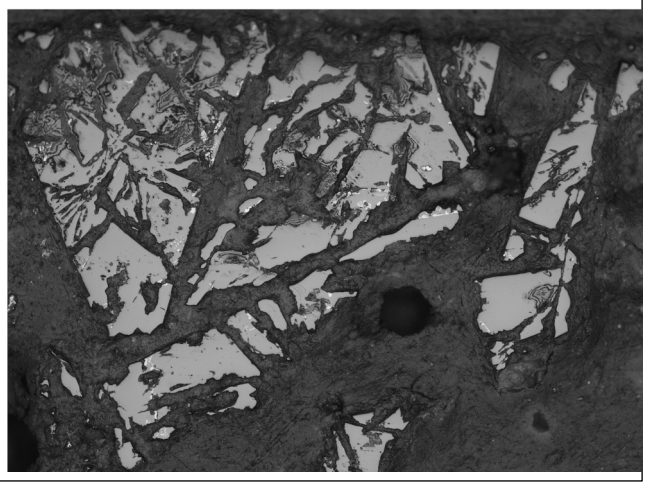

Figure 5 - Optical microstructure after infusing liquid Nb into B_4C at greater than 2477°C.

form no oxides. In a few crucibles, elemental components were melted together to create an alloy, which were then added in a follow-up melt heat.

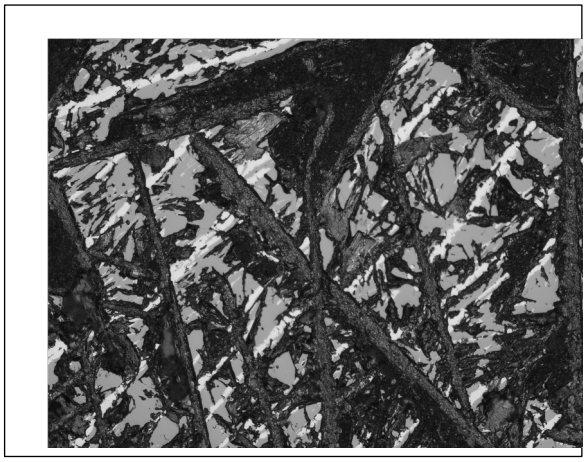

Figure 6 - Optical microstructure after infusing liquid Hf-Ti alloy into B_4C at greater than 2477°C.

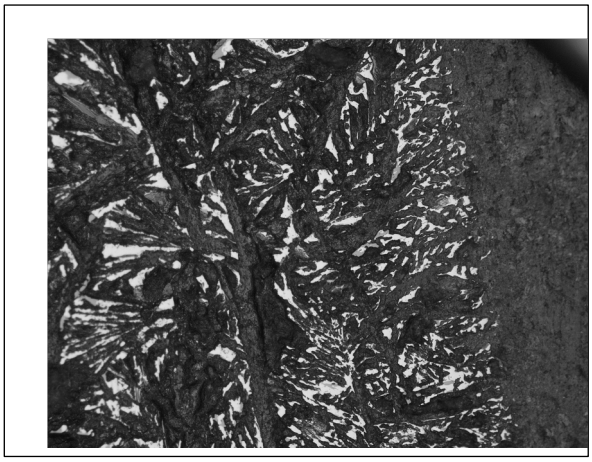

Figure 7 - Optical microstructure after infusing liquid 60Hf-40Nb-10Ti alloy into B_4C at greater than 2477°C.

The phases within the microstructure were not fully identified, yet, though they will be analyzed with X-ray diffraction (XRD) followed-up with scanning electron microscope – energy dispersive X-ray spectroscopy (SEM-EDXS) in the next stage of the research. The XRD will determine phases and whether any oxide was formed because the oxygen potential and thus experiments will then transition into a two-zone configuration as described for Figure 1. Also, available binary and ternary phase diagrams from the literature (e.g., NIST-JAmCeram database) are used to establish correctly the phases in the microstructure, as well as using calculated stability diagrams (e.g., Nb-C-O system) at the experimental temperature. The reaction path is M_xB_y-Me_rC_s-B_4C with the stoichiometry of the M borides and Me carbides depending on the compound formation with Hf, Nb, and Ti. Acicular formation of the borides would be minimized by adding carbon to prepare a B_4C-C mixture and precipitate a globular, rectangular or less acicular morphology contingent on the growth of the carbide at temperature.

2.4 Effects of Temperature: An accurate placement of the measuring pyrometer was a challenge especially since the calibration of the pyrometer with a Pt wire (melting temperature of 1768°C) and the positioning of the pyrometer onto a sighting cavity or an annulus sector was attempted simultaneously during measurement. The radiation emitted obscured the Pt wire so techniques were changed to view timely the Pt melting, but the concern was the accurate measurement of the temperature of the inner crucibles shown in Figure 4. The outer crucible was cut to form a annulus sector allowing measurement of the temperature axially and radially for the surfaces of the inner crucibles and the outer crucible. However, the adjustment of the pyrometer to measure the temperature of both surfaces will be solved in the next stage of the research. The researchers view the temperature measurement as very critical to determining the progress of the reactions.

Although the effect of a temperature gradient on the surface tension could explain the fluid flow into a porous media, irreversible thermodynamics with the phenomenological equations using

gradients and mobility coefficients could also analyze the behavior. For example, with considering only a temperature (T), the fluxes (J_i) with mole composition (N_i) will have the following form:

$$J_i = -\frac{D_i N_i}{RT^2}\left(H_i^M + Q_i^*\right)\frac{dT}{dx}$$

The terms in parenthesis symbolizing the partial molar enthalpy of solution (H_i^M) and the heat of transport (Q_i^*) could change the sign of the flux, though usually the temperature gradient (dT/dx) increases the flux of the species. It is hypothesized that the temperature gradient segregates the elemental components (i.e., Hf, Ta, Nb, B and C) corresponding to the hot and cold sides of temperature. For example, a steep temperature gradient will segregate the B and/or C elements to the cold side, for which superhard alloy surfaces can be exploited. The extent of the segregation with dT/dx will be investigated in the next stage of the research.

2.5. Objectives Achieved: The objectives met during the research effort:

1. The simulation of liquid Ti infusion into a packed bed was published in Metallurgical and Materials Transactions B in 2019.
2. The study of the effect of the contact angle, reaction kinetics for Ti liquid movement and contact line friction on the imbibing rate of liquid Ti into a capillary was simulated and a manuscript (appended) is in the final stages of preparation prior to submittal to Metallurgical and Materials Transactions B.
2. The infusion of liquid Hf, Zr and Ti was simulated with computations performed by using an in-house software, Exa-Scale Pore-Elastic Network Simulator (EXPNS), which incorporates efficient the Directed Acyclic Graph (DAG) for efficiency, modified nodal analysis algorithm for speed, and Trilinos and Dakota for massively parallel implementation and Uncertainty Quantification (UQ).
3. The induction furnace facility installation was completed and experiments with the Hf-Ti-Nb alloy melt reacting with B_4C at temperatures greater than 2477°C have started. A temperature of 2477°C was attained, because we melted Nb which has a melting temperature of 2477°C.

2.6. Future Goals: The research tasks possible for the project are as follows:

1. Characterize the reactive infused B_4C samples with XRD and SEM-EDXS to determine the reaction path of the $(Hf\text{-}Nb\text{-}Ti)_{Liq}/B_4C$ and to minimize formation of acicular borides.
2. Expand the extended finite volume code to incorporate the boride and carbide precipitates.
3. Extend the experimental temperatures greater than 2500°C with the induction furnace facility.
4. Check temperature measurements with the use of radiative cavities primarily made from graphite crucibles and acoustic emission to determine accurately the effect of the temperature gradient on the surface tension.
5. Link the penetration rate to the contact angle coupled with the surface tension as well as the temperature gradient.
6. Expand the exascale software to incorporate surface tensions of ternary liquid alloy compositions.

3. Accomplishments/New Findings

Accomplishments – Three journal publications have resulted from the research effort for the past year, as summarized in Section 5**.** The investigation has developed the exascale computer code to simulate the fluid dynamics of reactive liquid metals (i.e., Hf, Ti, Y and Zr) through the pores with a size distribution from 1 to 10 μm within a packed bed. The depth and rate of penetration were predicted with uncertainty quantification acquired to assess statistically the simulations. In addition, an algorithm was developed to predict machine learning

Relevance to Air Force Mission -- The computational fluid dynamics of the infusion of Hf alloy melts could optimize the placement of precipitates to improve mechanical and oxidizing properties for HfB_2/HfC/Hf-Ti-Nb at temperatures greater than 2000°C. The effects of surface energies, diffusion of components within the liquid phase, and interfacial reactions could be used to optimize the reactive infusion process. With the use computational fluid dynamics in liquid processing of boride/carbide systems at temperatures greater than 2000°C, the processing simulations of ceramic composites could predict the formation of stable and metastable phases to more extreme ultrahigh temperatures upon coupling of the modeling with thermodynamics.

4. Personnel Supported

Dr. Sanjay Shantha-Kumar is primarily supported by AFOSR funds. Sanjay Shantha-Kumar's primary responsibility was building and establishing an induction furnace facility for the experimental part of the study to verify the computational efforts. Laura Sandoval aided Dr. Shantha-Kumar with the experimental tasks but was limited with time because of her other duties involved in investigations with Dr. Ramana on the processing of thermoelectric materials and with Dr. Kumar's computational effort. Laura Sandoval was funded from the NSF Center for Materials Research during the academic year and the AFOSR project during the summer. Arturo Rodriguez, an undergraduate in the Department of Mechanical Engineering, aided Arturo Schiaffino, as well as Dr. V. M. Krushnarao Kotteda (University of Wyoming) who collaborates and works on a Department of Energy project with the exascale simulations with Dr. Vinod Kumar.

5. Publications/Interactions

In **Metallurgical and Materials Transactions B (2019, Vol. 50B, pp. 1559-1565)**, the paper entitled "Sensitivity of Viscosity on Molten Ti Infusion into a B_4C-Packed Bed at the Microscale" (V M Krushnarao Kotteda, Arturo Schiaffino, Ashesh Chattopadhyay, Shantha-Kumar Sanjay, Vinod Kumar, and Arturo Bronson) was published.

In **Powder Technology**, the paper entitled "Uncertainty Quantification of Fluidized Beds Using a Data-Driven Framework was published (V. M. Krushnarao Kotteda, J. Adam Stephens, W. Spotz, V. Kumar and A. Kommu, 2019, Vol. 354, pp. 709-718) as contributed by Drs. Kotteda and Kumar.

With the FactSage thermodynamic software/database funded by AFOSR, publication consisted of: V. Zade, B. Mallesham, S. Shantha-Kumar, A. Bronson, and C. V. Ramana, "Interplay between Solubility Limit, Structure, and Optical Properties of Tungsten Doped Ga_2O_3 Compounds Synthesized by a Two-Step Calcination Process," **Inorganic Chemistry**, 2019, Vol. 58, 3707-3716.

The paper appended and entitled "An Analysis of the Effect of Contact Angle on the Liquid Metal Infusion into a Packed Bed" was published on-line (2021, hard-copy will follow) in

Metallurgical and Materials Transactions B . Chris Harris of Shell Oil, Krushnarao Kotteda of University of Wyoming, Sanjay Shantha-Kumar (UTEP) and Arturo Bronson (UTEP) are the co-authors.

For the **conference papers** and presentations, the following were made:

1. A Schiaffino, Sanjay Shantha-Kumar, V Kumar, A Bronson, VMK Kotteda, **"**Uncertainty quantification of molten Hafnium infusion into a B_4C packed bed", Proceedings of the ASME-JSME-KSME Joint Fluids Engineering Conference 2019, San Francisco, USA.
2. A Schiaffino, Sanjay Shantha-Kumar, V Kumar, A Bronson, VMK Kotteda, "Predicting the depth of Penetration of molten metal into a pore network using Tensor flow", Proceedings of the ASME 2018 5th Joint US-European Fluids Engineering Summer Conference FEDSM 2018, Jul 2018, Montreal, Canada.
3. Z Nieto, Sanjay Shantha-Kumar, V Kumar, A Bronson, VMK Kotteda, "Utilization of Machine Learning to Predict the Surface Tension of Metals and Alloys", Proceedings of the ASME 2018 5th Joint US-European Fluids Engineering Summer Conference FEDSM 2018, Jul 2018, Montreal, Canada

6. Patent Disclosures/Awards

A patent was issued by the Patent Office with US patent No.10266739 in April 2019, entitled Compositions, Devices, Systems and Methods for Concentrating Solar Power. The calculations made with thermodynamic FactSage software/database which was funded by AFOSR was the basis for the patent.

7.References

1. Zhao J-C, Westbrook JH. Ultrahigh-Temperature Materials for Jet Engines. *MRS Bull*. 2003;28(09):622–630.
2. Petla H, Renova EP, Bronson A, Chessa JF, Maheswaraiah N. A computational analysis of a ZrO2–SiO2 scale for a ZrB_2–ZrC–Zr ultrahigh temperature ceramic composite system. *J Eur Ceram Soc*. 2010;30(11):2407–2418.
3. Bronson A, Chessa J. An Evaluation of Vaporizing Rates of SiO_2 and TiO_2 As Protective Coatings for Ultrahigh Temperature Ceramic Composites. *J Am Ceram Soc*. 2008;91(5):1448–1452.
4. Saiz E, Tomsia APAP. Atomic dynamics and Marangoni films during liquid-metal spreading. *Nat Mater*. 2004;3(12):903–909.
5. Saiz E, Hwang CW, Suganuma K, Tomsia a. P. Spreading of Sn-Ag solders on FeNi alloys. *Acta Mater*. 2003;51(11):3185–3197.
6. Grigorenko N, Poluyanskaya V. In Interfacial Sci. of Ceram. Joining, Bellosi et al, editors. *"In Interfacial Sci Ceram Joining, Bellosi al, Ed*. 1998;58:69–78.
7. Stolen, Svein, Grande, Tor, Allan N. Chemical Thermodynamics of Materials. New York: Elsevier Science Publishers; 2004.
8. Benhassine M, Saiz E, Tomsia APP, De Coninck J, Coninck J De. Nonreactive wetting kinetics of binary alloys: A molecular dynamics study. *Acta Mater*. 2011;59(3):1087–

1094.
9. Swiler TP, Loehman RE. Molecular dynamics simulations of reactive wetting in metal–ceramic systems. *Acta Mater*. 2000;48(18–19):4419–4424.
10. Delgado P, Kumar V. A stochastic Galerkin approach to uncertainty quantification in poroelastic media. *Appl Math Comput*. 2015;266:328–338.
11. Delgado P, Kumar V. Generalization of a heterogenous multiscale framework coupling discrete microscale and continuous macroscale physics in a porous medium. *ASME 2013 …*. 2013;V01CT23A001.
12. Kumar V, Harris CK, Bronson A, Shantha-Kumar S, Medina A. High-Temperature Liquid Metal Infusion Considering Surface Tension-Viscosity Dissipation. *Metall Mater Trans B*. 2016;47(1):108–115.
13. Semlak, K.A.Rhines FN. The rate of infiltration of metals. *Trans Met Soc AIME*. 1958;21:325–331.
14. Mortensen A, Jin I. Solidification processing of metal matrix composites. *Int Mater Rev*. 1992;37(1):101–128.
15. Garcia-Cordovilla C, Louis E, Narciso J. Pressure infiltration of packed ceramic particulates by liquid metals. *Acta Mater*. 1999;47(18):4461–4479.
16. Molina JM, Piñero E, Narciso J, García-Cordovilla C, Louis E. Liquid metal infiltration into ceramic particle preforms with bimodal size distributions. *Curr Opin Solid State Mater Sci*. 2005;9(4):202–210.
17. Blunt MJ. Flow in porous media - Pore-network models and multiphase flow. *Curr Opin Colloid Interface Sci*. 2001;6:197–207. https://doi.org/10.1016/S1359-0294(01)00084-X
18. Christie M, Demyanov V, Erbas D. Uncertainty quantification for porous media flows. *J Comput Phys*. 2006.
19. Maximenko AL, Olevsky EA. Pore filling during selective laser melting - assisted additive manufacturing of composites. *Scr Mater*. 2018;149:75–78.
20. Bakke S, Øren P. 3-D pore-scale modelling of sandstones and flow simulations in the pore networks. *Spe J*. 1997.
21. Morris JP, Zhu Y, Fox PJ. Parallel simulations of pore-scale flow through porous media. *Comput Geotech*. 1999.
22. Shalf J, Dosanjh S, Morrison J. Exascale Computing Technology Challenges. In: Palma JMLM, Daydé M, Marques O, Lopes JC, eds. *High Perform. Comput. Comput. Sci. -- VECPAR 2010*. Berlin, Heidelberg: Springer Berlin Heidelberg; 2011:1–25.
23. Bergman K, Borkar S, Campbell D, *et al.* Exascale computing study: Technology challenges in achieving exascale systems. 2008
24. Heroux M, Bartlett R, Howle V. An overview of the Trilinos project. *ACM Trans*. 2005.
25. Carter Edwards H, Trott CR, Sunderland D. Kokkos: Enabling manycore performance portability through polymorphic memory access patterns. *J Parallel Distrib Comput*. 2014;74(12):3202–3216. h
26. Adams BM, Bohnhoff WJ, Dalbey KR. DAKOTA, a multilevel parallel object-oriented framework for design optimization, parameter estimation, uncertainty quantification, and sensitivity analysis: *Sandia Natl*. 2009.
27. Akhmatskaya E, Todd BD, Daivis PJ. A study of viscosity inhomogeneity in porous media. *J*. 1997.
28. Jakeman J, Eldred M, Xiu D. Numerical approach for quantification of epistemic uncertainty. *J Comput Phys*. 2010;229(12):4648–4663.

29. Adams BM, Ebeida MS, Eldred MS, *et al.* Dakota, a multilevel parallel object-oriented framework for design optimization, parameter estimation, uncertainty quantification, and sensitivity analysis version 6.0 theory manual. Sandia National Lab.(SNL-NM), Albuquerque, NM (United States); 2014
30. Martins GP, Olson DL, Edwards GR. Modeling of infiltration kinetics for liquid metal processing of composites. *Metall Trans B*. 1988;19(1):95–101.
31. Ligenza JR, Bernstein RB. The Rate of Rise of Liquids in Fine Vertical Capillaries. *J Am Chem Soc*. 1951;73(10):4636–4638.
32. Kumar V, Harris C, Bronson A, Shantha-Kumar S, Medina A. High-Temperature Liquid Metal Infusion Considering Surface Tension-Viscosity Dissipation. *Metall Mater Trans B*. 2015;1–8.
33. Paradis P-F, Ishikawa T, Lee G-W, *et al.* Materials properties measurements and particle beam interactions studies using electrostatic levitation. *Mater Sci Eng R Reports*. 2014;76:1–53.
34. Ishikawa T, Paradis P-F, Okada JT, Watanabe Y. Viscosity measurements of molten refractory metals using an electrostatic levitator. *Meas Sci Technol*. 2012;23(2):025305.
35. Massalski TB, Okamoto H, Subramanian PR, Kacpack L. Binary Alloy Phase Diagrams. 2nd. Editi. Metals Park: ASM Internaitonal; 1990
36. Paradis P-F, Ishikawa T, Koike N. Thermophysical Properties of Molten Yttrium Measured by Non-contact Techniques. *Microgravity Sci Technol*. 2009;21(1–2):113–118.
37. S. Shantha-Kumar, Reaction of Liquid Aluminum-Samarium Alloys with B_4C at Ultra High Temperatures, ETD Collection for University of Texas, El Paso, 2015.

ORIGINAL RESEARCH ARTICLE

An Analysis of the Effect of Contact Angle on the Liquid Metal Infusion into a Packed Bed

CHRISTOPHER K. HARRIS, V.M. KRUSHNARAO KOTTEDA, SANJAY SHANTHA-KUMAR, VINOD KUMAR, and ARTURO BRONSON

In considering the dynamic wetting of liquid metal infusion into a packed bed, the effect of the contact angle on the penetrating rate and distance was analyzed by examining the momentum balance of the liquid within a capillary, as well as reactive and non-reactive processes occurring in the vicinity of the contact line. A numerical solution for liquid titanium infusing into a 10 μm radius cylindrical capillary reported previously was extended to include the effect of contact line friction, which has a significant influence at early times when meniscus velocities are high, and the reaction of the titanium with the substrate which takes effect at longer times and is assumed to decrease the contact angle. The contact line friction reduces the maximum meniscus velocities previously reported, while the increase in penetration depth during the reaction of the liquid metal with the substrate interpolates between the theoretical results for contact angles corresponding to fully unreacted and fully reacted substrates.

https://doi.org/10.1007/s11663-021-02065-1

I. INTRODUCTION

THE dynamics of liquid metal reactive wetting on metals and ceramics often include an initial spreading that precedes the onset of reaction between the liquid and the underlying substrate. In a previous study, the present authors[1] examined the dynamics of liquid titanium, yttrium, hafnium, samarium, and zirconium ingress into a packed ceramic bed by treating a pore entrance into the bed as a fine capillary tube extending the Semlak–Rhines equation.[2] The Semlak–Rhines relation was applied to liquid metals (*e.g.*, copper at 1098 °C to 1140 °C, 1371 K to 1413 K) and has the same form as the Lucas–Washburn–Rideal (LWR) equation originally established for water and organic solutions.[3–5] The original observation of a capillary penetration length changing with the square root of time and explanation for it in terms of a balance of capillary and viscous forces is due to Bell and Cameron,[6] whose experiments involved water, alcohol, and benzene.

CHRISTOPHER K. HARRIS is with the Department of Earth Science and Engineering, Imperial College London, South Kensington Campus, London SW7 2AZ, UK. Contact e-mail: ckh@imperial.ac.uk V.M. KRUSHNARAO KOTTEDA is with the Center of Innovation for Flow in Porous Media, University of Wyoming, 1000 E University Ave, Laramie, WY 82071. Contact e-mail: vkotteda@uwyo.edu, kvmkrao@gmail.com SANJAY SHANTHA-KUMAR, VINOD KUMAR, and ARTURO BRONSON are with the Department of Mechanical Engineering, The University of Texas at El Paso, 500 W University Ave, El Paso, TX 79968.

Manuscript submitted September 19, 2020; accepted December 23, 2020.

In our previous study,[1] an analysis was done using a modified form of the LWR valid for times less than 0.001 second with a maximum velocity of liquid titanium decreasing from 7 to 2.7 m/s into a 10 μm diameter pore for a contact angle increasing from 0 to 80 deg, respectively. The maximum velocity occurs between 1 and 10 μs depending on the contact angle for liquid titanium, yttrium, hafnium, samarium, and zirconium for a non-reactive penetration.

For the initial stages of spreading, Kumar and Prabhu,[7] Saiz et al.,[8] and Eustathopoulos[9] have reviewed the changes in the contact angle of the Young–Dupre equation. The Young–Dupre equation assumes a non-reactive interface and relates the surface tensions along with the solid/gas interface (σ_{SG}), solid/liquid interface (σ_{SL}), and liquid/gas interface (σ_{LG}) according to a force balance (*i.e.*, $\sigma_{SG} = \sigma_{SL} + \sigma_{LG}\cos(\theta)$). However, liquid metals may react with the substrate changing the contact angle and typically decreasing with time. For reaction-limited wetting, Dezellus *et al.*[10] proposed an exponential decay of the cosine of the contact angle with time as follows:

$$\cos(\theta) = \cos(\theta_\infty) - \{\cos(\theta_\infty) - \cos(\theta_0)\}\exp\left[-\frac{t}{t_R}\right] \quad [1]$$

where the logarithm of the difference between the initial contact angle (θ_0) and the final contact angle (θ_∞) *vs.* time (t) gives a slope of $1/t_R$. The behavior of Eq. [1] agreed with the data for sessile drops of liquid Cu40Si alloys placed onto a graphite substrate at temperatures ranging from 1373 K (1100 °C) to 1523 K (1250 °C).

Published online: 22 February 2021

For the reactive mode, a product layer or sometimes even layers form usually corresponding to compounds expected from a phase diagram though metastable phases may form upon cooling (*e.g.*, Ti-Nb alloys[11,12]). However, the initial stages of wetting incorporate the dissolution of the substrate, reaction of the liquid with the substrate, the movement of the liquid across the substrate as a result of inertia, end drag, and viscous flow. Saiz *et al.*[13] reported that the wetting also depends on the liquid/substrate chemical interactions affected by temperature. As a consequence, the dissolved oxygen within the liquid metal affects the contact angle along with the surface tension caused by the adsorption of active surface species, as reported by Gallois and Lupis.[14]

Blake and Haynes,[15] later reviewed by Blake,[16] developed an expression for the velocity (dL/dt) described as molecular kinetic theory (MKT). The theory assumes molecule moves on a substrate at an amplitude of displacement (λ) between adsorption sites with a characteristic frequency (k^o) and establishes a relation between the dynamic contact angle θ_D, the static contact angle θ_S, and the contact line velocity:

$$\frac{dL}{dt} = 2k^o\lambda \sinh\left[\frac{\sigma_{LG}\lambda^2}{2k_BT}(\cos\theta_S - \cos\theta_D)\right] \qquad [2]$$

The dynamic contact angle refers to the liquid spreading toward a final value, or static contact angle of θ_S, (sometimes termed equilibrium contact angle) and the other symbols refer to the Boltzmann constant (k_B) and temperature (T). If the argument of the sinh function is small (*i.e.*, $2k_BT \gg \sigma_{LG}\lambda^2(\cos\theta_S - \cos\theta_D)$), the velocity becomes:

$$\frac{dL}{dt} = k^o\lambda^3\left[\frac{\sigma_{LG}}{k_BT}(\cos\theta_S - \cos\theta_D)\right] \qquad [3]$$

Blake termed the quantity $\zeta = k_BT/(k^o\lambda^3)$ the contact line friction factor.

Benhassine *et al.*[17] used molecular dynamics (MD) to validate the MKT theory for Cu-Ag alloys and reported on a decreasing trend of the contact angle from initially about 160 deg to plateauing toward 30 deg within 5 ns. In the review of MD simulations to wetting, De Coninck and Blake[18] reported on contact angles of a liquid imbibing into a capillary within a 5 ns to 1 second time frame. They also evaluated the coefficient of contact line friction, which appears to become a contributory factor at high wetting speeds and times less than 1 second. Saiz and Tomsia[19] observed wetting speeds ranging from 0.1 to 1 m/s for liquid Cu and Au on Mo substrate. Also, Saiz *et al.*[20] have reported on the velocity of liquid copper and gold spreading on nickel decreasing linearly with increasing contact angle with the slope related to the wetting- or contact line friction ranging from 1 to 2 Pa-s.

For reactive dynamic wetting, the contact angle initially may depend on the rate of reaction between the liquid metal (*i.e.*, Ti) and the substrate (C or B_4C), the solubility of the elemental components of the substrate within the liquid metal, and the possible ensuing formation of a reaction product (*e.g.*, TiC), as reviewed by Aizenshtein, Froumin, and Frage.[21] Whether the liquid metal spreads for brazing of ceramic surfaces or infuses into the pores of a packed bed of non-metallic particles, the initial dynamic wetting of the liquid seems to attain velocities greater than 1 m/s initially, although for a time greater than 10 μs they decrease substantially and follow the inverse dependence on the square root of time as described in Semlak and Rhines.[2] Eustathopolus,[9] who also reported on liquid alloys on carbide and oxide substrates, shows the usual decreasing trend of the contact angles with time for reactive and non-reactive systems. Although the decreasing trend of the contact angle is usually considered related to a kinetic process, the objective of the present study is to compare the kinetics of the rate-determining reaction with the contact line friction.

In the following section, the theoretical aspects of the penetration of liquid metal into a packed bed combine the fundamental concepts of fluid mechanics and chemical reactivity. The development involves first a momentum balance of the fluid infusing the packed bed. Afterward, a reaction sequence for an atom to jump away from liquid onto a vacancy or defect to spread the dynamic wetting across the substrate. The section closes with the conversion into a dimensionless representation of the equation.

II. THEORETICAL BASIS

A. *Fluid Mechanics*

Consider the geometry shown in Figure 1, where a tube of internal radius R contains a liquid meniscus with contact angle θ. Subsidiary quantities are the angle α and meniscus radius r_m and defined as follows:

$$\alpha = \frac{\pi}{2} - \theta \qquad [4]$$

and

$$r_m = \frac{R}{\sin(\alpha)} \qquad [5]$$

It then follows that

$$h_o = r_m\{1 - \cos(\alpha)\} = R\frac{\{1 - \cos(\alpha)\}}{\sin(\alpha)} \qquad [6]$$

The volume V_L of the liquid contained within the two planes, represented by horizontal dashed lines in Figure 1, is given by

$$V_L = \pi R^2 h_o - \left\{\frac{2\pi}{3}\{1 - \cos(\alpha)\}r_m^3 - \frac{1}{3}(\pi R^2)r_m\cos(\alpha)\right\}$$
$$= \frac{1}{3}\pi R^3\frac{\{(1 - \cos(\alpha)\}^2(1 + 2\cos(\alpha))}{\sin^3(\alpha)} \qquad [7]$$

In terms of the contact angle θ, we have, using Eq. [4]

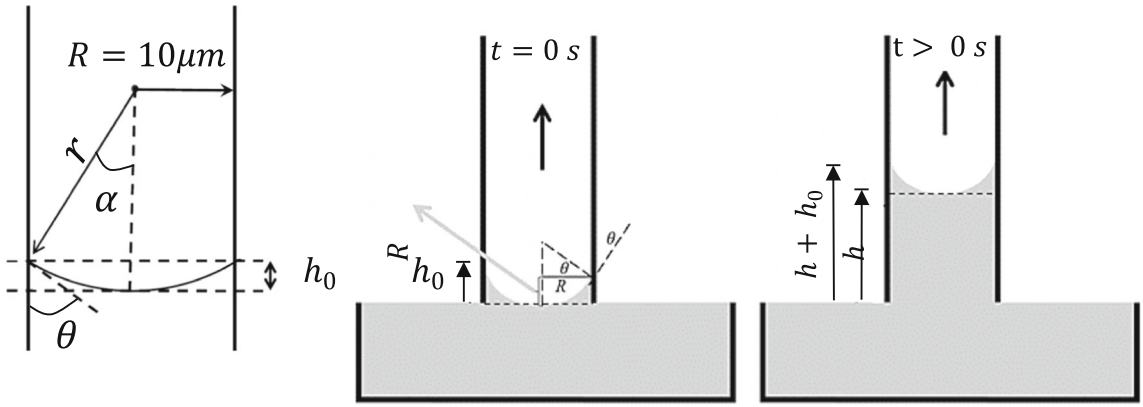

Fig. 1—Capillary tube is lowered onto the surface of a liquid that wets the tube. (Left) Liquid interface arranges to an equilibrium capillary shape when the bottom of the tube contacts the liquid. (Right)[1] Liquid imbibes into tube under the influence of capillary forces.

$$V_{\mathrm{L}} = \frac{1}{3}\pi R^2 \frac{\{(1-\sin(\theta)\}^2(1+2\sin(\theta))}{\cos^3(\theta)} \qquad [8]$$

Furthermore,

$$h_{\mathrm{o}} = R\frac{(1-\sin(\theta))}{\cos(\theta)} \qquad [9]$$

We also introduce the quantity h_{L}, given by

$$h_{\mathrm{L}} = \frac{V_{\mathrm{L}}}{\pi R^2} \qquad [10]$$

At equilibrium, the capillary rise height h_{e} is given by

$$h_{\mathrm{e}} = \frac{2\sigma\cos(\theta)}{\rho g R} \qquad [11]$$

The height of the capillary at time t depends on the conservation of momentum as similarly developed by Kumar *et al.*[1] and is given by the rate of momentum accumulation equated to terms consisting of forces of the surface tension with the contact angle (θ), viscosity (μ), gravity (g), and end drag as follows:

$$\frac{\mathrm{d}}{\mathrm{d}t}\left(\rho\pi R^2 h + \rho V_{\mathrm{L}}\right)\frac{\mathrm{d}h_{\mathrm{col}}}{\mathrm{d}t} = 2\pi R\sigma\cos(\theta) - 8\pi\mu\left(h + h_{\mathrm{o}} + \frac{1}{4}R\chi\right)\frac{\mathrm{d}h}{\mathrm{d}t} - \rho\pi R^2 hg - \int \rho\pi R^2\left(\frac{\mathrm{d}h_{\mathrm{col}}}{\mathrm{d}t}\right)^2 \qquad [12]$$

where $h_{\mathrm{col}} = h + h_{00} - h_0 + h_{\mathrm{L}}$ is the average height of the liquid column from the base of the capillary tube to the liquid–vapor meniscus. Here, h_{00} is the initial value of h_0. Equation [12] is subject to the boundary conditions (Eq. [4] from Reference 1)

$$h(0) = 0; \quad \left.\frac{\mathrm{d}h}{\mathrm{d}t}\right|_{t=0} = 0 \qquad [13]$$

The quantity χ appearing in the second term on the right-hand side of Eq. [12] is the contact line friction coefficient and is related to the contact line friction factor ζ introduced below Eq. [3] by $\zeta = \mu\chi$. In general, the range of friction coefficient is from 10 to 1000.[22]

Equation [12] is similar to Eq. [3] of Reference 1, except that h_0 in the drag term on the right-hand side is augmented by ¼ $R\chi$, and the pre-factor of 1/4 in the end drag, or entrance effect, the term is replaced by ε. This is to accommodate other authors who have argued the values 0[23,24] or 1/6[25] as being the most appropriate value for ε. The value $\varepsilon = 1/4$ was adopted by Wang *et al.*[26]

In the non-reactive case, the contact angle θ is assumed to be constant (and less than 90 deg so that the liquid metal wets the solid). For the reactive case, the contact angle is assumed to decrease with time from a value $\theta = \theta_{\mathrm{o}}$ to $\theta = \theta_{\infty}$ according to Eq. [1]. The force incorporating the surface tension with the contact angle is referred to sometimes as the capillary force as termed by Blake.[16]

B. *Reaction Sequence*

Although the dynamics of the contact angle were explained according to Eq. [1], a possible reaction sequence is proposed here for simplicity with a graphite substrate though a similar sequence may be developed for a C or a B_4C substrate. The initial dynamic wetting is assumed to occur under a reaction-controlled process without the bulk diffusion of components for the movement of the three-phase line consisting of liquid, solid, and gas. A reaction sequence involving liquid metal adsorbing onto the surrounding substrate could occur in steps similar to the adsorption–desorption steps developed similarly by Grabke and Horz[27] and Wang *et al.*[28] for gases adsorbing onto metals. Similarly, liquid titanium (Ti_{L}) adsorbing onto the surrounding surface of a substrate starts initially with Ti atoms moving on the surface according to the following reaction.

$$Ti_{\mathrm{L}} = Ti_{\mathrm{Sur}} \qquad [14]$$

The physically adsorbed Ti on the surface (Ti_{Sur}) will move on the substrate and combines with an empty site (V) such as a surface defect, vacancy, or kink to create adsorbed Ti (Ti_{Ads}) according to the following reaction:

$$V + Ti_{Sur} = Ti_{Ads} \quad [15]$$

The adsorbed Ti will than combine with carbon exposed on the surface to form TiC as follows:

$$Ti_{Ads} + C = TiC + V \quad [16]$$

The movement of Ti, its combination with a vacancy to create an adsorbed Ti species, is shown in Figure 2. If the reaction causing the formation of an adsorbed Ti is the rate-determining step for the reaction sequence, the rate (r_2) for Ti adsorption is proportional to the moles/area of adsorbed Ti ($n_{Ti,Ads}$) and with the rate constant (k_2) for reaction [15] the rate equation is deduced as:

$$r_2 = \frac{dn_{Ti,Ads}}{dt} = k_2 n_{Ti,Ads} \quad [17]$$

After rearranging, the integration from an initial Ti moles/area content ($n^{o}_{Ti,ads}$) to Ti moles/area at the time (t) as $n^{t}_{Ti,ads}$ yields the following result:

$$\int_{n^{o}_{Ti,ads}}^{n^{t}_{Ti,ads}} \frac{dn_{Ti,Ads}}{n_{Ti,Ads}} = \int_{0}^{t} k_2 dt \quad [18]$$

Integrating and setting a time constant $\tau_R = (k_2)^{-1}$, the concentration of the adsorbed Ti becomes

$$n_{Ti,ads} = n^{o}_{Ti,ads} e^{t/\tau_R} \quad [19]$$

The rate-determining step (Eq. [15]) of the reaction sequence is converted into a wetting velocity (dL/dt) of the moving titanium liquid by the density of titanium (ρ_{Ti}) and atomic mass (M_{Ti}) as follows:

$$M_{Ti} \frac{dn_{Ti,Ads}}{\rho_{Ti} dt} = \frac{dL}{dt} \quad [20]$$

The wetting velocity or rate of adsorption converted to the adsorbed Ti ($n_{Ti,Ads}$) and dL/dt (or dh/dt) is substituted, the foregoing equation becomes:

$$M_{Ti} \frac{dn_{Ti,Ads}}{\rho_{Ti} dt} = \frac{dL}{dt} = \frac{dh}{dt} = \left(\frac{k_2 M_{Ti}}{\rho_{Ti}}\right) n^{o}_{Ti,ads} e^{t/\tau_R} \quad [21]$$

$$\frac{dh}{dt} = \left(\frac{k_2 M_{Ti}}{\rho_{Ti}}\right) n^{o}_{Ti,ads} e^{t/\tau_R} \quad [22]$$

The foregoing equation shows that the imbibing rate depends on the exponential of time for the adsorption of Ti_{Ads} atoms (onto the immediate surrounding area of the liquid titanium (Ti_L).

C. *Dimensionless Parameters*

Note that V_L and h_o, as well as h_e will also depend on t as they are functions of θ. We will assume that $\theta_\infty < \theta_o < \pi/2$ in this study with a comment on other cases at the end. We introduce equilibrium capillary rise heights corresponding to contact angles θ_0 and θ_∞ by

$$h_{eo} = \frac{2\sigma\cos(\theta_0)}{\rho g R}; \quad h_{e\infty} = \frac{2\sigma\cos(\theta_\infty)}{\rho g R} \quad [23]$$

We introduce the non-dimensional time $\tilde{t}$ and capillary rise height $\tilde{h}$ by

$$\tilde{t} = t\sqrt{\frac{g}{h_{e\infty}}}; \quad \tilde{h} = \frac{h}{h_{e\infty}}; \quad \tilde{h}_L = \frac{h_L}{h_{e\infty}}; \quad \tilde{h}_{col} = \frac{h}{h_{e\infty}}; \quad \tilde{h}_0 = \frac{h_0}{h_{e\infty}} = \tilde{R}\frac{1-\sin(\theta)}{\cos(\theta)}; \quad \tilde{R} = \frac{R}{h_{e\infty}} \quad [24]$$

In terms of these, Eq. [12] may be rewritten as

$$\begin{aligned} h_{e\infty} g \frac{d}{d\tilde{t}} \left\{ \left(\rho\pi R^2 \tilde{h}_{col}\right) \frac{d\tilde{h}_{col}}{d\tilde{t}} \right\} &= 2\pi R\sigma\cos(\theta) \\ &- 8\pi\mu\sqrt{h_{e\infty} g} h_{e\infty} \left(\tilde{h} + \tilde{h}_0 + \frac{1}{4}\tilde{R}\chi\right) \frac{d\tilde{h}}{d\tilde{t}} \\ &- h_{e\infty}\rho\pi R^2 \tilde{h} g - \varepsilon h_{e\infty} g \rho\pi R^2 \left(\frac{d\tilde{h}_{col}}{d\tilde{t}}\right)^2 \end{aligned} \quad [25]$$

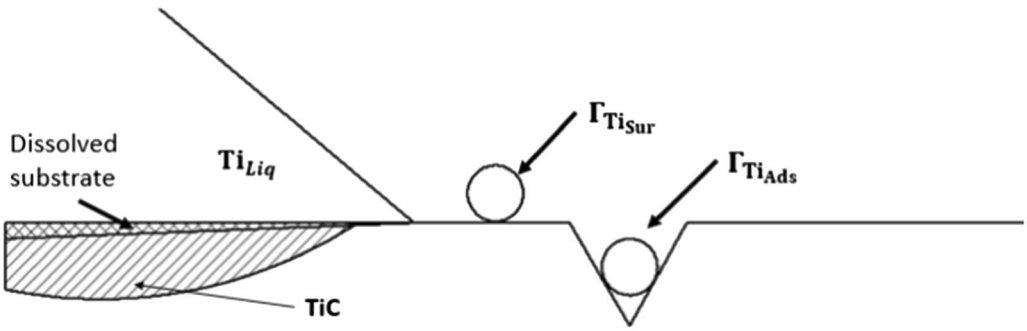

Fig. 2—Sketch of the movement of a titanium atom from the liquid titanium onto the surface of the substrate to combine with a vacancy to form an adsorbed titanium atom.

Note that θ_S has simply been written as θ in Eq. [25]. Dividing Eq. [25] by $\rho g \pi R^2 h_{e\infty}$(assuming that ρ is constant), we obtain

$$\frac{\mathrm{d}}{\mathrm{d}\tilde{t}}\left\{\left(\tilde{h}+\tilde{h}_L\right)\frac{\mathrm{d}\tilde{h}_{\mathrm{col}}}{\mathrm{d}\tilde{t}}\right\}=\frac{2\sigma\cos(\theta)}{\rho g R h_{e\infty}} - 8\tilde{\mu}\left(\tilde{h}+\tilde{h}_0+\frac{1}{4}\tilde{R}\chi\right)\frac{\mathrm{d}\tilde{h}}{\mathrm{d}\tilde{t}}-\tilde{h} - \varepsilon\left(\frac{\mathrm{d}\tilde{h}_{col}}{\mathrm{d}\tilde{t}}\right)^2 \quad [26]$$

where $\tilde{\mu}=\mu\frac{h_{e\infty}}{\rho R^2\sqrt{g\,h_{e\infty}}}$.

Substituting Eq. [23] into Eq. [26] and making use of Eq. [24], we obtain

$$\frac{\mathrm{d}}{\mathrm{d}\tilde{t}}\left\{\tilde{h}_{\mathrm{col}}\frac{\mathrm{d}\tilde{h}_{\mathrm{col}}}{\mathrm{d}\tilde{t}}\right\}=1-\left(1-\tilde{h}_{e0}\right)\exp\left(-\frac{\tilde{t}}{\tilde{t}_{\mathrm{R}}}\right) - 8\tilde{\mu}\left(\tilde{h}+\tilde{h}_0+\frac{1}{4}\tilde{R}\chi\right)\frac{\mathrm{d}\tilde{h}}{\mathrm{d}\tilde{t}}-\tilde{h} - \varepsilon\left(\frac{\mathrm{d}\tilde{h}_{\mathrm{col}}}{\mathrm{d}\tilde{t}}\right)^2 \quad [27]$$

where $\tilde{h}_{e0}=h_{e0}/h_{e\infty}; \quad \tilde{t}_{\mathrm{R}}=t_{\mathrm{R}}\sqrt{g/h_{e\infty}}$

D. *Numerical Solution*

It is convenient to scale the dimensionless meniscus height and time as follows:

$$\tilde{h}=\tilde{h}_{\mathrm{L0}}\tilde{H}; \quad \tilde{t}=\tilde{T}\tilde{h}_{\mathrm{L0}} \quad [28]$$

Here, $\tilde{h}_{\mathrm{L0}}$ is the value of $\tilde{h}_{\mathrm{L}}$ at the initial contact angle θ_0. Then Eq. [27] can be written as

$$\frac{\mathrm{d}}{\mathrm{d}\tilde{T}}\left\{\tilde{H}_{\mathrm{col}}\frac{\mathrm{d}\tilde{H}_{\mathrm{col}}}{\mathrm{d}\tilde{T}}\right\}=1-\left(1-\tilde{h}_{e0}\right)\exp\left(-\frac{\tilde{T}}{\tilde{T}_{\mathrm{R}}}\right) - \beta\left(\tilde{H}+\tilde{H}_{0,\mathrm{eff}}\right)\frac{\mathrm{d}\tilde{H}}{\mathrm{d}\tilde{T}}-\tilde{H}\tilde{h}_{\mathrm{L0}} - \varepsilon\left(\frac{\mathrm{d}\tilde{H}_{\mathrm{col}}}{\mathrm{d}\tilde{T}}\right)^2 \quad [29]$$

where $\tilde{H}_{\mathrm{L}}$,$\tilde{H}_0$, $\tilde{H}_{\mathrm{col}}$, $\tilde{T}_{\mathrm{R}}$, and β are given by

$$\tilde{H}_{\mathrm{L}}=\frac{\tilde{h}_{\mathrm{L}}}{\tilde{h}_{\mathrm{L},0}}; \quad \tilde{H}_0=\frac{\tilde{h}_0}{\tilde{h}_{\mathrm{L0}}}; \quad \tilde{H}_{\mathrm{col}}=\frac{\tilde{h}_{\mathrm{col}}}{\tilde{h}_{\mathrm{L},0}}; \quad \tilde{T}_{\mathrm{R}}=\frac{\tilde{t}_{\mathrm{R}}}{\tilde{h}_{\mathrm{L0}}};_4\,\beta=8\mu\tilde{h}_{\mathrm{L0}}; \quad \tilde{H}_{0,\mathrm{eff}}=\tilde{H}_0+\frac{1}{4}\frac{R}{h_{\mathrm{L0}}}\chi \quad [30]$$

We perform the numerical solution for liquid titanium, at its melting temperature of 1668 °C, infusing into a 10 μm radius cylindrical capillary composed of B_4C. The surface tension and density of the liquid metal were taken to be 1.555 N m^{-1} and 4.17 kg m^{-3}, respectively,[29] while the viscosity used was 3.3 $(10)^{-3}$ kg m^{-1} s^{-1}, extrapolating data from Ishikawa *et al.*[30] We do this first for the non-reacting case, so that the static and final contact angles are equivalent ($\theta_0 = \theta_\infty$). Then Eq. [29] becomes

$$\frac{\mathrm{d}}{\mathrm{d}\tilde{T}}\left\{\left(\tilde{H}+1\right)\frac{\mathrm{d}\tilde{H}}{\mathrm{d}\tilde{T}}\right\}=1-\beta\left(\tilde{H}+\tilde{H}_{0,\mathrm{eff}}\right)\frac{\mathrm{d}\tilde{H}}{\mathrm{d}\tilde{T}}-\tilde{H}\tilde{h}_{\mathrm{L0}} - \varepsilon\left(\frac{\mathrm{d}\tilde{H}}{\mathrm{d}\tilde{T}}\right)^2 \quad [31]$$

subject to the boundary conditions (Eq. [4] from Reference 1)

$$\tilde{H}(0)=0; \quad \left.\frac{\mathrm{d}\tilde{H}}{\mathrm{d}\tilde{T}}\right|_{\tilde{T}=0}=0 \quad [32]$$

Note that, in writing Eq. [31], we have neglected the effect of the changing meniscus shape on the liquid column height and have simply taken $\tilde{H}_{\mathrm{L}}$ to be unity. Three different contact angles are considered, as shown

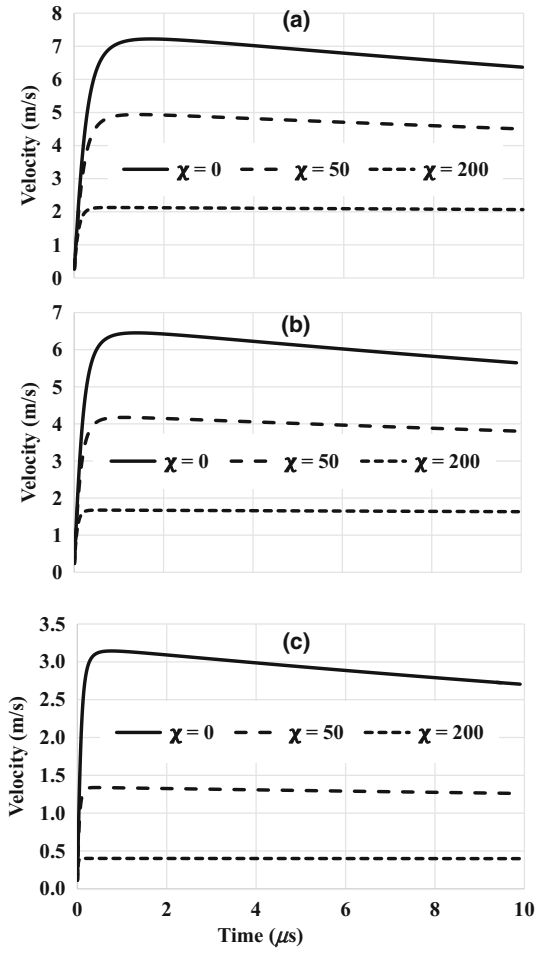

Fig. 3—Velocity of the initial capillary rise for liquid titanium with values of the contact line friction coefficient (χ) at the melting point into a 10 μm radius capillary of B_4C: (*a*) equilibrium contact angle θ = 0 deg, (*b*) θ = 40 deg, and (*c*) θ = 80 deg.

Table I. Geometrical and Associated Parameters Depending on the Contact Angle for Titanium Melt Infusing into Capillary Tube of B_4C with a Radius of 10 mm

θ (deg)	h_L (μm)	h_0 (μm)	H_0	h_e(m)	$\tilde{\mu}$	β
0	3.33	10	3	7.60	6966	0.0244
20	2.92	7.00	2.39	7.14	6753	0.0221
40	2.16	4.66	2.16	5.82	6097	0.0181
60	1.31	2.68	2.05	3.80	4926	0.0135
80	0.436	0.874	2.01	1.32	2903	0.00768

in Figures 3(a) through (c). To acquire a sense of the geometrical and associated parameters for the contact angles, parameters are summarized in Table I.

Equation [31] is marched forward according to $U = d\tilde{H}/d\tilde{T}$

Let $\tilde{T}_k$, U_k, and $\tilde{H}_k$ denote the values of $\tilde{T}$, U, and $\tilde{H}$ at step k. Then

$$\tilde{H}_{k+1} = \tilde{H}_k + U_k\left(\tilde{T}_{k+1} - \tilde{T}_k\right) \quad [33]$$

$$\begin{aligned}(\tilde{H}_{k+1}+1)U_{k+1} = &(\tilde{H}_k+1)U_k \\ &+\left\{1-\tilde{h}_{L0}\tilde{H}_k-\beta\left(\tilde{H}_k+C\right)U_k-\varepsilon U_k^2\right\} \\ &\left(\tilde{T}_{k+1}-\tilde{T}_k\right)\end{aligned} \quad [34]$$

The timesteps are chosen according to the following rule:

$$\tilde{T}_k = k\Delta\tilde{T}; \quad k = 0, 1 \ldots n \quad [35]$$

$$\tilde{T}_k = n\Delta\tilde{T}\left\{1+\frac{1}{n}\right\}^{k-n}; \quad k = n, n+1 \ldots N \quad [36]$$

III. RESULTS

The meniscus velocity for the three contact angles is shown in Figure 3. We take $\Delta\tilde{T} = 0.00001$ and $n = 1000$. For each contact angle, the numerical calculation is run to 1000 μs.

Figure 3(a) shows the results of the calculations of the meniscus velocity for the three contact angles, where the entrance effect of 1/4 ($\varepsilon = 1/4$), $\chi = 0$ and the corresponding values of β and H_0 are given in Table I. Exact solutions of Eq. [31], subject to Eq. [32], are available for $\tilde{H}_0 = 1$, $\chi = 0$ and $\varepsilon = 0$ and/or $\beta = 0$. The sensitivity of meniscus velocity to the friction factor for three different contact angles can be seen in Figures 3(a) through (c). The velocity decreases with an increase in the friction factor as well as the contact angle. We also studied the entrance/end effects on the maximum meniscus velocity for the three contact angles (see Figure 4). These show a decrease with an increase in the contact line friction with a modest effect of the choice of the end-drag coefficient ε. The relative contribution of the force due to the contact line friction (CLF) on the infiltration of the liquid metal is divided by the surface force (or capillary force) and shown in Figure 5. As expected, since this force (CLF) is proportional to velocity, but not infiltration length (as is the case for the viscous drag), it rises to a maximum and then falls off.

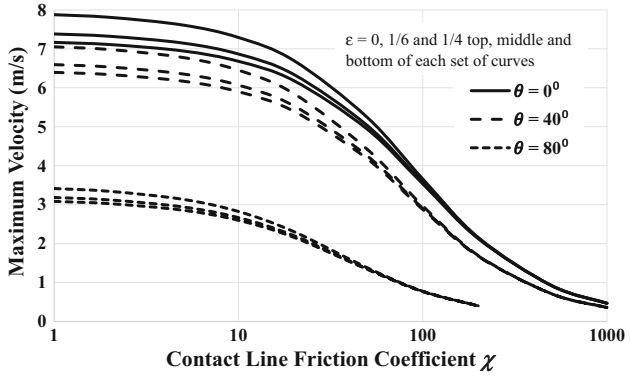

Fig. 4—Maximum meniscus velocity for liquid Ti, at melting point, as a function of friction coefficient ε. The effect of different values of the end-effect coefficient ε is also shown.

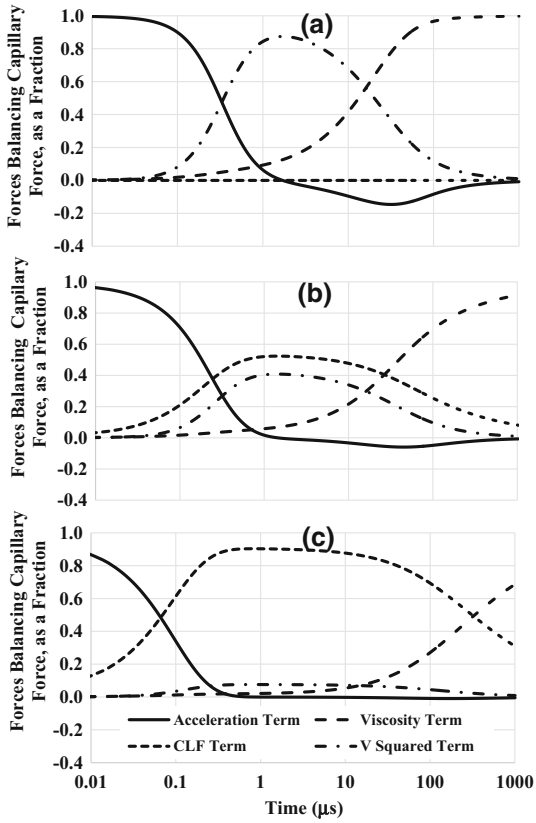

Fig. 5—Relative contributions of the acceleration, viscosity, contact line friction (CLF), and velocity squared terms in balancing the capillary force, for the rise of liquid titanium, at the melting point, in a 10 μm radius B_4C capillary with an equilibrium contact angle of 0 deg. (*a*) $\chi = 0$, (*b*) $\chi = 50$, and (*c*) $\chi = 200$.

List of Symbols and their Units—(a) Roman Symbols

Parameter Description	Symbol	Unit
Height h Normalized with Respect to h_{L0}	$\tilde{H}$	—
Meniscus Extent h_0 Normalized with Respect to h_{0L}	$\tilde{H}_0$	—
Effective Normalized Meniscus Extent = $(h_0 + ¼ R\chi)/h_{L0}$	$\tilde{H}_{0,eff}$	—
h_L Normalized with Respect to its Initial Value	$\tilde{H}_L$	—
$\tilde{H}$ at Timestep k	$\tilde{H}_K$	—
Capillary Radius	R	m
Absolute Temperature	T	K
Time t Normalized with Respect to $(h_{L0}/h_{e,\infty})\sqrt{(h_{e,\infty}/g)}$	$\tilde{T}$	—
Reaction Time t_R Normalized with Respect to $(h_{L0}/h_{e,\infty})\sqrt{(h_{e,\infty}/g)}$	$\tilde{T}_R$	—
$\tilde{T}$ at Timestep k	$\tilde{T}_k$	—
Normalized Velocity: dh/dt Divided by $\sqrt{(h_{e,\infty}g)}$	U	
U at Timestep k	U_k	—
Volume of Liquid Above Meniscus Base	V_L	m^3
Acceleration due to Gravity (9.81)	g	m s^{-2}
Meniscus Height	h	m
Meniscus Height Normalized with Respect to Capillary Rise Height	$\tilde{h}$	—
Height of Contact Line Above Base of Meniscus	h_0	m
h_0 Normalized with Respect to Capillary Rise Height	$\tilde{h}_0$	—
V_L Divided by Capillary Cross-Sectional Area	h_L	m
h_L Normalized with Respect to Capillary Rise Height	$\tilde{h}_L$	-
h_L at Initial Contact Angle θ_0	h_{L0}	m
h_{L0} Normalized with Respect to Capillary Rise Height	h_{L0}	—
Capillary Rise Height for Contact Angle Remaining at θ_0	h_{e0}	m
h_{e0} Normalized with Respect to Capillary Rise Height	$\tilde{h}_{e0}$	—
Capillary Rise Height	$h_{e\infty}$	m
Characteristic Frequency of Molecular Motion	k^0	s^{-1}
Reaction Rate	k_2	s^{-1}
Boltzmann's Constant (1.381×10^{-23})	k_B	kg m^2 s^{-2} K^{-1}
Moles per Unit Area of Adsorbed Titanium	n	m^{-2}
Initial Moles per Unit Area of Adsorbed Titanium	n^0	m^{-2}
Radius of Meniscus Surface	r_m	m
Time	t	s
Time Normalized with Respect to $\sqrt{(h_{e,\infty}/g)}$	$\tilde{t}$	—
Reaction Time Scale in Eq. [1]	t_R	s
t_R Normalized with Respect to $\sqrt{(h_{e,\infty}/g)}$	$\tilde{t}_R$	—

List of Symbols and their Units—(b) Greek Symbols

Parameter Description	Symbol	Unit
Normalized Viscosity $8h_{L0}\mu\{\rho R^2\sqrt{(h_{e,\infty}g)}\}$	β	—
End-effect Coefficient	ε	—
Contact Line Friction Factor	ζ	kg m^{-1} s^{-1}
Contact Angle	θ	—
Initial Contact Angle	θ_0	—
Equilibrium Contact Angle	θ_∞	—
Dynamic Contact Angle	θ_D	—
Static Contact Angle	θ_S	—
Atomic Displacement Amplitude	λ	m
Liquid Viscosity	μ	kg m^{-1} s^{-1}
Normalized Viscosity $h_{e\infty}\mu\{\rho R^2\sqrt{(h_{e,\infty}g)}\}$	$\tilde{\mu}$	—
Liquid Density	ρ	kg m^{-3}
Liquid–Vapor Surface Tension	σ	kg s^{-2}
Liquid–Vapor Surface Tension	σ_{LG}	kg s^{-2}
Solid–Vapor Surface Tension	σ_{SG}	kg s^{-2}
Solid–Liquid Surface Tension	σ_{SL}	kg s^{-2}
Reaction Time Constant (= $1/k_2$)	τ_R	s
Contact Line Friction Factor Coefficient	χ	—

At the maximum meniscus velocity, inertial force is negligible, and the V-squared term (or $(dh/dt)^2$) is a maximum.

Extending the calculations to the reacting case, we use the example of titanium melt infusing into a 10 μm radius B_4C capillary tube as before, and take $\theta_0 = 80$ deg, $\theta_\infty = 0$ deg. We explore the effect on the meniscus velocity profile of varying T_R. It is useful to note that

$$\frac{h_L}{h_e} = \frac{\rho g R^2 (1-\sin(\theta))^2 (1+2\sin(\theta))}{6\sigma\cos^4(\theta)} = \frac{\rho g R^2 (1+2\sin(\theta))}{6\sigma(1+\sin(\theta))^2} \quad [37]$$

We further have

$$\tilde{h}_L = \frac{h_L}{h_{e\infty}} = \frac{\rho g R^2 (1-\sin(\theta))^2 (1+2\sin(\theta))}{6\sigma\cos^4(\theta)} = \frac{\rho g R^2 (1+2\sin(\theta))}{6\sigma(1+\sin(\theta))^2}\frac{\cos(\theta)}{\cos(\theta_\infty)} \quad [38]$$

The results for the dynamic case are shown for various values of τ_R in Figure 6. Numerical benchmarking of the solution for reactive infusion was performed by taking advantage of the fact that, if the gravity and end-effect terms are removed (*i.e.*, ε is set to zero) from Eq. [29], and H_o is set equal to H_L, the equation may be integrated once analytically.

The short-time behavior will be characteristic of the behavior of a non-reactive melt with contact angle θ_0, and the effect of the reaction will become evident in the LWR or Semlak–Rhines part of the meniscus velocity *vs.* time curve. Here, inertial terms and the end effect may be neglected, and Eq. [31] reduces to

$$0 = \left(1 - \tilde{h}_{L0}\right) \exp\left(-\frac{\tilde{T}}{\tilde{T}_R}\right) - \beta\left(\tilde{H} + \tilde{H}_0\right) \frac{d\tilde{H}}{d\tilde{T}} - \tilde{H}\tilde{h}_{L0} \quad [39]$$

Equation [39] is valid for some $\tilde{T} > T_S$, where, certainly, $\beta T_s \gg 1$. If $T_R \ll T_S$, the exponential term can be neglected and H_o can be replaced by $H_{o\infty}$. In that case, the Semlak–Rhines behavior is the same as for the non-reactive case with contact angle θ_∞. For T_R comparable to or larger than T_S, there is a cross-over behavior that we now examine. Let us take $t_S = 10^{-2}$ second and choose t_R of 10, 50, 100, 200, and 1000 seconds. Rewriting Eq. [27] in terms of $\tilde{h}$ and $\tilde{t}$ we obtain

$$0 = \left(1 - \tilde{h}_{e0}\right) \exp\left(-\frac{\tilde{t}}{\tilde{t}_R}\right) - 8\tilde{\mu}\left(\tilde{h} + \tilde{h}_0\right) \frac{d\tilde{h}}{d\tilde{t}} - \tilde{h} \quad [40]$$

Equation [40] is solved for $\tilde{t} > \tilde{t}_s$. subject to $\tilde{h}_{\tilde{t}=\tilde{t}_s} = \tilde{h}_s$. The value of $\tilde{h}_s$. to be used is determined from the solution of Eq. [29]. For the case of liquid titanium melt with an initial contact angle $\theta_0 = 80$ deg, $t_S = 10^{-2}$ second corresponds to $\tilde{T} = 82477.39$.

The above calculations were performed for infusing reactive liquid metal with an initial contact angle θ_0 and a finite contact angle θ_∞ such that $\theta_\infty \le \theta_0 < \pi/2$. While the literature indicates that reaction renders the liquid metal more wetting to the solid (*i.e.*, $\theta_\infty < \theta_0$), it is also possible to have $\theta_\infty < \pi/2 < \theta_0$. In this case, the reaction proceeds without infusion until the contact angle reaches $\pi/2$, at which point the infusion starts.

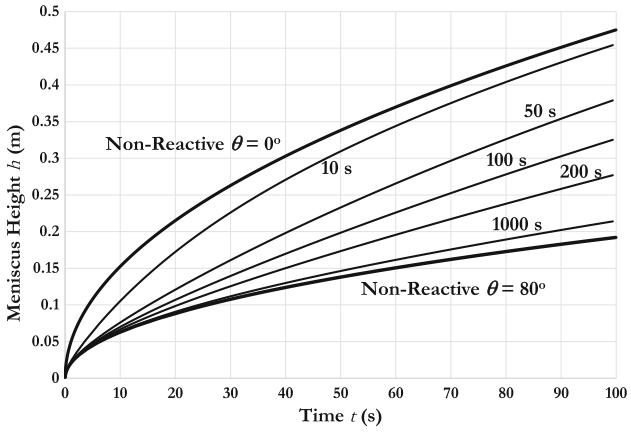

Fig. 6—The effect of reaction time constant (t_R) on the meniscus height for titanium melt infusing into a 10 μm radius capillary tube. The initial and final contact angles are 80 and 0 deg, respectively. The bold curves are the results for a non-reactive melt with contact angles of 0 and 80 deg. Here, $\varepsilon = 0$ and $\chi = 1/4$.

IV. DISCUSSION

This work presents three extensions to our previous paper[1] on liquid metal infusion into a porous solid comprising of B_4C particles. The first extension is the inclusion of a contact line friction term related to adsorption of the liquid metal onto the interface, which is significant compared with the drag due to viscosity in the early stages of capillary rise when the liquid column is short, and the velocities are high. The drag coefficient χ is assumed to be in the range 10 to 1000, in accordance with literature studies,[22] and reduces the maximum velocity, as shown in Figures 3(a) through (c), which depict the velocity *vs.* time for three different values of the friction coefficient, and in Figure 4, which shows the maximum velocity *vs.* χ. Also, for a second extension as there has been some debate in the literature, the effect of varying the entrance effect coefficient ε was investigated and was found to be fairly modest for values less than ¼ considered.

Relative contribution of the forces acceleration, contact line friction, viscosity, and end drag divided by the capillary force or balancing the driving capillary action is shown in Figure 5. The forces of acceleration and capillary action are clearly significant at time less than 1 μs. The viscosity and capillary forces increase with increasing time beyond approximately 50 μs though the end drag and contact line friction become prevalent between 1 and 50 μs depending on the contact line friction coefficient (χ).

The third extension is the inclusion of a reaction between the liquid metal and the ceramic preform, which has the effect of lowering the contact angle. Dezellus, Hodaj, and Eustathopoulos[31] reported the product layer as a thin layer of SiC formed between Cu-Si liquid and C substrate. They reported that in the initial time span, the contact angle decreases rapidly followed by a slower linear rate. Another consideration is the time span of the product layer forming between the liquid and substrate. Aizenshtein *et al.*[21] reported the product layer of TiC_x and TiB_x forming also behind the triple line or between the dissolved Ti in a Cu-Ti liquid and the B_4C substrate. They also reported a microstructure showing liquid Ti contacting directly B_4C between the produce layer and the triple line at the juncture of the liquid Ti/B_4C and atmosphere. The liquid Ti/B_4C interface infers that the product layer of TiC_x or TiB_x does not form immediately upon the contact of liquid Ti with B_4C, but the product layer evolves by nucleation and growth, as reported by Saiz *et al.*[13]

The analysis resulting from the calculations in Figure 6 shows a reaction timescale assumed to be of the order of 1 to 100 seconds. In addition, the results show a dependence of the liquid penetrating distance *vs.* time that interpolates between those of an unreacted and completely reacted 10-μm radius tube according to the reaction timescale of less than 100 seconds, as shown in Figure 6, where unreacted and completely reacted contact angles are assumed to be 80 and 0 deg,

respectively. The results do indicate that the reacting product shifting the time constant may increase the contact angle causing the penetrating height to decrease.

V. CONCLUSIONS

In considering the dynamic wetting of liquid metal infusion into a packed bed, the effect of the contact angle on the penetrating rate and distance was analyzed by examining the momentum balance of the liquid within a capillary, as well as reactive and non-reactive processes occurring in the vicinity of the contact line. If the advancing front of liquid Ti on a substrate, prior to the onset of the reaction of Ti with the B_4C to form TiC and TiB_2, is assumed to depend on the rate-determining step of the adsorption of Ti onto a surface defect (*e.g.*, vacancy), the dynamic contact angle θ_D becomes controlled by the rate constant of the reaction for adsorption and leads to an effective contact line friction. The imbibing rate of the liquid into a pore increases with decreasing static contact angle θ_s with a maximum velocity near 1 μs for the micrometer-sized capillary considered here. This maximum velocity decreases with increasing contact line friction. Later on, at times t of the order of 1 to 1000 seconds, a decrease in contact angle θ_s due to the presence of the reaction products TiC and TiB_2 results in a penetration depth that follows a rough $t^{1/2}$ dependence interpolating between the theoretical results for a fully unreacted and fully reacted substrate.

ACKNOWLEDGMENTS

This material was based on research sponsored by the Air Force Research Laboratory, under Agreement Number FA9550-17-1-0393, FA9550-19-1-0304, FA9550-17-1-0253, and FA9550-12-1-0242 through the Air Force Office of Scientific Research (AFOSR) and is gratefully acknowledged with the support of Dr. Ali Sayir, Stacie Williams, Brett Pokines, and Edward Lee of AFOSR. The work is partially supported by Department of Energy (DE-FE0026220, DE-FE0002407, NETL, Sandia, ORNL, NREL), and Systems Plus. We would also like to thank NSF (HRD-1139929, XSEDE Award Number ACI-1053575), TACC, DOE, DOD HPCMP, University of Texas STAR program, UTEP (Research Cloud, Department of Mechanical Engineering, Graduate School & College of Engineering) for generously providing financial support or/and computational resources. Without their generous support, it would have been almost impossible to complete the milestones. The US Government is authorized to reproduce and distribute reprints for governmental purposes notwithstanding any copyright notation thereon. The views and conclusions contained herein are those of the authors and should not be interpreted as necessarily representing the official policies or endorsements, either expressed or implied, of the Air Force Research Laboratory or the US Government. The authors would like to thank the anonymous referees for their constructive comments, which improved the clarity of the paper.

REFERENCES

1. V. Kumar, C.K. Harris, A. Bronson, S. Shantha-Kumar, and A. Medina: *Metall. Mater. Trans. B*, 2016, vol. 47B, pp. 108–15.
2. K.A. Semlak and F.N. Rhines: *Trans. TMS-AIME*, 1958, vol. 212, pp. 325–31.
3. R. Lucas: *Kolloid-Zeitschrift*, 1918, vol. 23, pp. 15–22.
4. E.W. Washburn: *Phys. Rev.*, 1921, vol. 17, pp. 273–83.
5. E.K. Rideal: *Lond. Edinburgh Dublin Philos. Mag. J. Sci.*, 1922, vol. 44, pp. 1152–59.
6. J.M. Bell and F.K. Cameron: *J. Phys. Chem.*, 1905, vol. 10, pp. 658–74.
7. G. Kumar and K.N. Prabhu: *Adv Colloid Interface Sci.*, 2007, vol. 133, pp. 61–89.
8. E. Saiz, R.M. Cannon, and A.P. Tomsia: *Annu. Rev. Mater. Res.*, 2008, vol. 38, pp. 197–226.
9. N. Eustathopoulos: *Metals*, 2015, vol. 5, pp. 350–70.
10. O. Dezellus, F. Hodaj, and N. Eustathopoulos: *J. Eur. Ceram. Soc.*, 2003, vol. 23, pp. 2797–803.
11. D.L. Moffat and U.R. Kattner: *Metall. Trans. A*, 1988, vol. 19A, pp. 2389–97.
12. M. Bönisch, M. Calin, T. Waitz, A. Panigrahi, M. Zehetbauer, A. Gebert, W. Skrotzki, and J. Eckert: *Sci. Technol. Adv. Mater.*, 2013, vol. 14, art. no. 055004.
13. E. Saiz, R.M. Cannon, and A.P. Tomsia: *Acta Mater.*, 2000, vol. 48, pp. 4449–62.
14. B. Gallois and C.H.P. Lupis: *Metall. Trans. B*, 1981, vol. 12B, pp. 549–57.
15. T.D. Blake and J.M. Haynes: *J. Colloid Interface Sci.*, 1969, vol. 30, pp. 421–23.
16. T.D. Blake: *J. Colloid Interface Sci.*, 2006, vol. 299, pp. 1–13.
17. M. Benhassine, E. Saiz, A.P.P. Tomsia, J. De Coninck, and J. De Coninck: *Acta Mater.*, 2011, vol. 59, pp. 1087–94.
18. J. De Coninck and T.D. Blake: *Annu. Rev. Mater. Res.*, 2008, vol. 38, pp. 1–22.
19. E. Saiz and A.P. Tomsia: *Curr. Opin. Solid State Mater. Sci.*, 2005, vol. 9, pp. 167–73.
20. E. Saiz, M. Benhassine, J. De Coninck, and A.P. Tomsia: *Scripta Mater.*, 2010, vol. 62, pp. 934–38.
21. M. Aizenshtein, N. Froumin, and N. Frage: *Engineering*, 2014, vol. 06, pp. 849–68.
22. D Duvivier, TD Blake, and J De Coninck: *Langmuir*, 2013, https://doi.org/10.1021/la4017917.
23. É. Lorenceau, D. Quéré, J.Y. Ollitrault, and C. Clanet: *Phys. Fluids*, 2002, vol. 14, pp. 1985–92.
24. O. Shardt, P.R. Waghmare, J.J. Derksen, and S.K. Mitra: *RSC Adv.*, 2014, vol. 4, pp. 14781–85.
25. J. Szekely, A.W. Neumann, and Y.K. Chuang: *J. Colloid Interface Sci.*, 1971, vol. 35, pp. 273–78.
26. Q. Wang, L. Li, J. Gu, and N. Weng: *Chem. Eng. Sci.*, 2019, vol. 209, art. no. 115220.
27. HJ Grabke and G Horz: *Annu. Rev. Mater. Sci.*, 1977, vol. 7, pp. 155–78.
28. P.W. Wang, J. Woo, M. Avila, J. Garcia, A. Bronson, and S.K. Varma: *J. Mater. Sci.*, 2003, vol. 38, pp. 489–97.
29. PF Paradis, T Ishikawa, GW Lee, D Holland-Moritz, J Brillo, WK Rhim, and JT Okada: *Mater. Sci. Eng. R Rep.*, 2014, vol. 76, pp. 1–53.
30. T. Ishikawa, P.-F. Paradis, J.T. Okada, and Y. Watanabe: *Meas. Sci. Technol.*, 2012, vol. 23, art. no. 025305.
31. O. Dezellus, F. Hodaj, and N. Eustathopoulos: *J. Eur. Ceram. Soc.*, 2003, vol. 23, pp. 2797–2803.